Exposed high-energy facets in ultradispersed sub-10 nm SnO_2 nanocrystals anchored on graphene for pseudocapacitive sodium storage and high-performance quasi-solid-state sodium-ion capacitors

Panpan Zhang[1,2], Xinne Zhao[2], Zaichun Liu[1,3], Faxing Wang[1,3], Ying Huang[4], Hongyan Li[5], Yang Li[2], Jinhui Wang[2], Zhiqiang Su[2], Gang Wei[6], Yusong Zhu[3], Lijun Fu[3], Yuping Wu[1,3] and Wei Huang[3]

Abstract

The development of sodium (Na) ion capacitors marks the beginning of a new era in the field of electrochemical capacitors with high-energy densities and low costs. However, most reported negative electrode materials for Na^+ storage are based on slow diffusion-controlled intercalation/conversion/alloying processes, which are not favorable for application in electrochemical capacitors. Currently, it remains a significant challenge to develop suitable negative electrode materials that exhibit pseudocapacitive Na^+ storage for Na ion capacitors. Herein, surface-controlled redox reaction-based pseudocapacitance is demonstrated in ultradispersed sub-10 nm SnO_2 nanocrystals anchored on graphene, and this material is further utilized as a fascinating negative electrode material in a quasi-solid-state Na ion capacitor. The SnO_2 nanocrystals possess a small size of <10 nm with exposed highly reactive {221} facets and exhibit pseudocapacitive Na^+ storage behavior. This work will enrich the methods for developing electrode materials with surface-dominated redox reactions (or pseudocapacitive Na^+ storage).

Introduction

Increasing interest in portable electronic devices, electric vehicles, and smart grids is creating significant demand for low-cost, environmentally friendly energy storage devices[1–4]. The electrochemical capacitor (also called supercapacitor) is one of the most promising energy storage devices, as it has a fast power delivery and long cycle life, although it still suffers from a moderate energy density compared with those of rechargeable batteries[5–7]. To improve the energy densities of electrochemical capacitors, lithium (Li) ion capacitors have been constructed from a capacitor-type electrode (such as activated carbon, carbon nanotubes (CNTs), and graphene) and a battery-type electrode (such as $Li_4Ti_5O_{12}$, TiO_2, Fe_3O_4, and Li_3VO_4) in a Li salt-containing electrolyte since 2001[2–16]. Li ion capacitors can achieve energy densities approaching those of Li ion batteries with power densities similar to those of electrochemical capacitors[17–23].

Correspondence: Faxing Wang (faxing.wang@tu-dresden.de) or
Zhiqiang Su (suzq@mail.buct.edu.cn) or Yuping Wu (wuyp@fudan.edu.cn)
[1]State Key Laboratory of Materials-Oriented Chemical Engineering, Nanjing Tech University, Nanjing 210009 Jiangsu Province, China
[2]State Key Laboratory of Chemical Resource Engineering, Beijing University of Chemical Technology, Beijing 100029, China
Full list of author information is available at the end of the article.
These authors contributed equally: Panpan Zhang, Xinne Zhao, Zaichun Liu.

Currently, Li ion capacitors ranging from lab-scale demonstrations to commercial products are being rapidly developed. For example, *Maxwell* and *CRRC Corporation Limited* have cooperated in the development of commercial Li ion capacitors, which have been utilized in the brake energy recovery system of a subway in China since 2016 (http://stock.10jqka.com.cn/20161129/c595244612.shtml). It is foreseeable that Li ion capacitors will become one of the most promising candidates for next-generation hybrid electric vehicles and pure electric vehicles. However, the enormous exploitation of Li resources driven by the ever-growing demands will eventually cause Li to become scarce. Consequently, replacing Li with Na to build an analogous Na ion capacitor offers an opportunity to construct a sustainable energy storage system with a high-energy density[24]. The technologies of Na ion capacitors based on liquid electrolytes have made significant advances in the past several years[24−30]. However, the liquid electrolytes for Na ion capacitors suffer from safety issues owing to their intrinsic instability in terms of flammability, possibility of leakage, and internal short circuit. Therefore, solid electrolytes would be a perfect choice to solve this crucial problem[31−33].

In addition to electrolytes, another key part of Na ion capacitors is the negative electrode, whose kinetics, which are based on a diffusion-controlled intercalation (or conversion or alloying) process, are slower than that of the positive electrode with a surface-controlled process (electric double-layer absorption/desorption). Currently, some negative electrode materials for Na ion capacitors have been reported. For example, Simon's and Yamada's groups fabricated two Na ion capacitors based on MXene (Ti_2C and V_2C) as negative electrodes, but these capacitors operated at relatively low voltages (<3.5 V) with a poor cycling stability (only 300 cycles)[27,28]. Two other fabricated Na ion capacitors based on V_2O_5 and TiO_2 as negative electrodes in liquid electrolytes could only be operated within low voltage ranges with low energy densities (both below 65 Wh kg^{-1} based on the total mass of the negative and positive electrodes)[25,29], which are not comparable with the high-energy density of conventional Li ion capacitors. By applying hard carbon with a low working potential as the negative electrode for Na ion capacitors, the energy density can be remarkably enhanced due to the expanded working voltage[31]. However, at a low potential (close to 0.1 V vs. Na^+/Na), both Na plating and the growth of dendrites take place on the negative electrode, which cause safety hazards and expose the device to a wide range of safety concerns. Very recently, $NaTi_2(PO_4)_3$ grown on graphene nanosheets was demonstrated as an intercalation negative electrode for Na ion capacitors[30]. When trapped between graphene layers, the electrical conductivity of the $NaTi_2(PO_4)_3$ nanoparticles (100 nm) greatly increased, thus enhancing the charge transfer kinetics and reducing the interfacial resistance at high current rates[30]. However, the reaction kinetics at the $NaTi_2(PO_4)_3$ electrode are still dominated by diffusion-controlled intercalation processes, which is inappropriate for electrochemical capacitors. Generally, the kinetics of a negative electrode based on a diffusion-controlled intercalation (or conversion or alloying) process are far slower than that of a positive electrode with a surface-controlled process. Fortunately, some traditional Li ion battery materials with diffusion-controlled processes in their bulk states can be utilized as extrinsic pseudocapacitive materials when they are reasonably designed through physical control of the electrode materials (including the particle size, surface area, electrical conductivity, morphology, and face orientation)[34−41]. These electrode materials (such as ordered mesoporous MoO_3 nanocrystals[34], mesoporous $Li_xMn_2O_4$ thin films[38], and oxygen vacancy-enhanced MoO_{3-x}[40] and $TiO^{2-}{}_x$[41]) display superior pseudocapacitive Li^+ storage behaviors, which should make them perfect choices for Li ion capacitors. However, few negative electrode materials (only TiO_2/graphene[42], SnS_2[43], and SnS nanosheets[44]) exhibit pseudocapacitive Na^+ storage behavior. The development of electrode materials with pseudocapacitive Na^+ storage properties is in the preliminary stage. Therefore, it remains a significant challenge to develop suitable negative electrode materials with surface-dominated pseudocapacitive Na^+ storage properties for Na ion capacitors.

Herein, we demonstrate that pseudocapacitive Na^+ storage instead of a diffusion-controlled reaction dominates the charge storage process in ultradispersed sub-10 nm SnO_2 nanocrystals with exposed {221} facets anchored on graphene. This nanocomposite of SnO_2/graphene can be prepared on a large scale by a facile one-step reaction with a hydrothermal method. It exhibits a high specific capacity of 276 F g^{-1} at a current density of 0.5 A g^{-1} and an excellent cycling stability of up to 6000 cycles. Even at a high current density of 1.8 A g^{-1}, this nanocomposite shows a specific capacitance of 105 F g^{-1}. Then, a quasi-solid-state Na ion capacitor is assembled using CNTs as the positive electrode and SnO_2/graphene as the negative electrode in a Na ion-conducting gel polymer electrolyte. The obtained quasi-solid-state Na ion capacitor displays a maximum energy density of 86 Wh kg^{-1} and a maximum power density of 4.1 kW kg^{-1}. After 900 cycles, this quasi-solid-state Na ion capacitor exhibits a stable capacitance retention of 100% at a current density of 0.5 A g^{-1}, which is competitive with those of current Na ion capacitors in liquid electrolytes.

Materials and methods

Synthesis of SnO₂/graphene

Graphene oxide (GO) was first synthesized by a modified Hummers method according to our previous work[45]. For the preparation of SnO_2 nanoparticles, 200 mg of $SnCl_2 \cdot 2H_2O$ was dissolved into 20 mL of deionized (DI) water and sonicated for 10 min to achieve a clear and homogeneous solution. After that, 200 mg of sodium citrate was added, and the mixture was further sonicated for 30 min. The solution was transferred to a 50 mL Teflon-lined autoclave and heated in an oven at 200 °C for 10 h with no intentional control of the ramping or cooling rate. To prepare SnO_2/graphene, 200 mg of $SnCl_2 \cdot 2H_2O$ was added to aqueous GO (0.5 mg mL⁻¹, 20 mL) and then sonicated for 10 min. After adding 200 mg of sodium citrate, the reaction solution was further sonicated for 30 min and then transferred to a 50 mL Teflon-lined autoclave. Then, it was heated at 200 °C for 10 h in an oven without intentional control of the ramping or cooling rate. The product was both centrifuged at 4500 rpm for 10 min with DI water and ethanol, and each washing step was repeated at least three times. Finally, the product was redisposed in 3 mL of DI water and freeze-dried for several days.

Synthesis of Na⁺ conducting gel polymer electrolyte (N-GPE)

The polymer matrix for N-GPE was prepared by a phase separation process[31]. Poly(vinylidene fluoride-*co*-hexafluoropropylene) (P(VDF-HFP)) with a molecular weight of approximately 329,000 (Supplementary Fig. S1) was dissolved in a mixture of *N,N*-dimethylformamide (DMF) and DI water at 80 °C with a mass ratios of P(VDF-HFP): DMF:H₂O = 15:85:3. The solution was cast onto a clean glass plate before being soaked in a water bath at 80 °C to form a homogeneous white membrane. After that, the white membrane was dried under vacuum at 100 °C for 10 h. Then, the obtained dry membrane was punched into circular pieces ($d = 19$ mm). Finally, the circular pieces were immersed in an organic electrolyte (1 mol L⁻¹ NaClO₄ solution in ethylene carbonate (EC)/dimethyl carbonate (DMC)/diethyl carbonate (DEC), 1/1/1, w/w/w) over 12 h in a glove box (water content: <1 ppm) to acquire the N-GPE. The amount of liquid electrolyte taken up (ΔW) was calculated according to the following equation:

$$\Delta W = \frac{100(W_s - W_o)}{W_o}\% \tag{1}$$

where W_o and W_s are the weights of the membrane before and after absorption of the organic electrolyte, respectively. In this work, the uptake of the liquid electrolyte is approximately 115 wt.%, which is enough to provide a high ionic conductivity.

Material characterization

High-resolution transmission electron microscopy (HRTEM) was conducted on a JEM-2100F field emission transmission electron microscope (JEOL products, Japan) at an acceleration voltage of 200 kV. The samples were prepared by dropping a SnO_2/graphene aqueous solution onto a copper grid and drying at room temperature. N_2 adsorption–desorption isotherms were obtained by the 3H-2000PS1 static volume method with a specific surface and pore analysis instrument (BeiShiDe, Beijing). Scanning electron microscopy (SEM, JSM-6700F, JEOL, Japan), X-ray diffraction (XRD, Rigaku D/max-2500 VB+/PC), X-ray photoelectron spectroscopy (XPS, ThermoVG ESCALAB 250), Fourier transform infrared (FTIR) spectroscopy (Nicolet 6700, Thermo-Fisher), and Raman spectroscopy (LabRAM HORIBA JY, Edison, NJ) were used to confirm the structures and morphologies of the SnO_2 nanoparticles, GO, and SnO_2/graphene.

Electrochemical measurement

Standard coin-type model cells were used to construct half cells. In the constructed half cells, Na metal served as the counter and reference electrodes, and the N-GPE functioned as the electrolyte. The specific capacitance (F g⁻¹) of the electrode material was obtained from the charge and discharge curves and calculated via the formula $C = (I\,\Delta t)/(m\,\Delta U)$, where I is the current (A) used for charge/discharge cycling, Δt is the charge time (seconds), m is the mass (g) of active materials in the working electrode, and ΔU is the operating potential range (V) during the charge process. Electrochemical measurements of the quasi-solid-state Na ion capacitor were conducted by using two-electrode cells at room temperature. The material (SnO_2/graphene or CNTs), carbon black, and polymer binder (polyvinylidene difluoride) with a weight ratio of 80:10:10 were assembled as active electrodes. The mass proportion of the electrode material was optimized by the equivalents of charge stored in a single electrode measurement. Generally, through the equation $q = C \times \Delta E \times m$ (C represents the specific capacitance in a half-cell test, ΔE is the voltage range, and m is the mass of the active material), the charge stored by each electrode can be determined. The N-GPE was utilized as the electrolyte and the separator. All cells were assembled in an Ar-filled glove box under oxygen and water concentrations below 1 ppm.

Density functional theory (DFT) calculations

The DFT-based first-principles calculations reported herein were performed with the CASTEP package of Materials Studio 6.0 within the generalized gradient approximation, as formulated by the Perdew–Burke–Ernzerhof functional[46,47]. The final set of energies for all calculations was computed with an energy cutoff of 370

eV. Adsorption-optimized structural modeling was performed using a $3 \times 3 \times 1$ supercell on the {110}, {001}, and {221} surfaces of SnO_2. All atoms were fully relaxed until the convergence criteria for energy were set to $10-5$ eV, and the residual forces on each atom decreased below 0.03 meV Å^{-1}. The linear synchronous-transit/quadratic synchronous-transit (LST/QST) method was used to perform migration energy barrier calculations within a large $2 \times 2 \times 2$ supercell[48]. The Brillouin zone integration was performed with $1 \times 1 \times 1$ and $2 \times 2 \times 4$ Γ-centered Monkhorst-Pack k-point meshes in geometry optimization and LST/QST calculations, respectively[49].

Results and discussion

The SnO_2/graphene nanocomposite was synthesized through a one-step hydrothermal reaction of few-layered GO (2–3 layers, 2–10 µm, Supplementary Fig. S2) and $SnCl_2 \cdot 2H_2O$ in an aqueous solution at 200 °C. In the starting material, the sharp diffraction peak observed at 9.68° in the XRD pattern is consistent with the characteristic diffraction peak (001) of GO. The diffraction peak of graphene exhibits a dramatic shift to a higher 2θ angle of ~28°, proving that GO was successfully reduced to graphene (Supplementary Fig. S3a). In addition, the increased intensity ratio of the D- and G-bands (I_D/I_G) of graphene relative that of GO in the Raman spectra indicates that most of the oxygenated groups were removed during the reduction process (Supplementary Fig. S3b). Meanwhile, due to the strong electrostatic interactions between Sn^{2+} and GO, SnO_2 nanocrystals are uniformly anchored on the surface of the graphene nanosheets. These SnO_2 nanocrystals enable independent dispersion of the graphene nanosheets without evident agglomeration (Fig. 1a and Supplementary Fig. S4), while the graphene can effectively restrict the further growth of SnO_2 nanocrystals (Fig. 1b, c). In comparison, without graphene, the pure SnO_2 crystals prepared under the same hydrothermal conditions exhibit a size >100 nm (Supplementary Fig. S5). The energy dispersive X-ray spectroscopy (EDX) mapping results show that Sn is uniformly dispersed on the graphene nanosheets (Supplementary Fig. S6), verifying the ultradispersed distribution of SnO_2 nanocrystals on the graphene surface.

A HRTEM image of SnO_2 nanocrystals is presented in Fig. 1d. The apex angle of the SnO_2 nanocrystals between two side surfaces is approximately 88° when viewed from the $[\bar{1}\,\bar{1}\,1]$ zone axis, in good agreement with the octahedral SnO_2 model enclosed by {221} facets projected along the same direction (Fig. 1e). The two sets of lattice fringes with spacings of 0.26 and 0.33 nm are in accordance with the (101) and (110) planes, respectively, of rutile SnO_2 (Fig. 1f). When some of the SnO_2 nanocrystals were rotated to the $[\bar{1}\,0\,1]$ zone axis from the $[\bar{1}\,\bar{1}\,1]$ zone

axis, as indexed by the selected-area electron diffraction pattern shown in Figure 1g, a perfect apex angle of approximately 65° between the two side surfaces also agrees well with the model of the octahedral SnO_2 enclosed by {221} facets projected along the same direction (Fig. 1h). The HRTEM image (Fig. 1i) shows that the lattice distances are 0.33 and 0.31 nm, corresponding to the (110) and (001) planes, respectively, of SnO_2. Based on the above TEM observations of different regions with different zone axes in the SnO_2 nanocrystals, it is concluded that the {221} facets are exposed in these nanocrystals. More micrographs showing the morphology of SnO_2/graphene can be found in Supplementary Fig. S7.

The XRD pattern of SnO_2 in the nanocomposite can be indexed to the tetragonal rutile phase of SnO_2 (JCPDS card no. 41–1445)[50], and no other Sn oxide phases are detected (Fig. 2a). Moreover, the intensity ratio of the (221) peak to the (110) peak of SnO_2/graphene is larger than that of the sample obtained without sodium citrate during the reaction, indicating that more exposed {221} facets are present in the SnO_2 nanocrystals of the nanocomposite. This suggests that environmentally friendly sodium citrate can be utilized as capping agent to obtain SnO_2 nanocrystals with exposed {221} facets. Actually, the surface energies of the SnO_2 facets follow the trend {110} < {100} < {101} < {001}[51]. This means that the {001} facet with the largest surface energy could possess the highest reactivity compared with the other crystal facets, thus promoting growth in the [001] direction. In this case, the SnO_2 nanocrystals tend to form surfaces enclosed by the thermodynamically most stable {110} facet in order to maintain the lowest surface energy. However, the surface energy can be strongly affected by the adsorption of foreign ions on the crystal facets. Here, DFT calculations show that citrate prefers to adsorb on the {221} facets, which have the most negative adsorption energy value (Fig. 2b) compared with those of the {110} and {001} facets, thus hindering crystal growth along the [221] direction and resulting in exposed {221} facets. For the parallel experiment without sodium citrate, anisotropic growth along the [221] direction is no longer suppressed, leading to the formation of irregular SnO_2 polycrystals that still have a sub-10 nm size (Supplementary Fig. S8). For another control sample without only GO, the obtained SnO_2 is bulk crystals with sizes up to several micrometers (Supplementary Fig. S5). Moreover, this bulk SnO_2 has a lower intensity ratio of the (221) peak to the (110) peak (Supplementary Fig. S9). Therefore, both GO and sodium citrate are indispensable for obtaining SnO_2 nanocrystals with exposed {221} facets. More specifically, the role of GO is to restrict further growth of the SnO_2 nanocrystals, while sodium citrate acts as a capping agent for exposing the {221} facets on the sub-10 nm
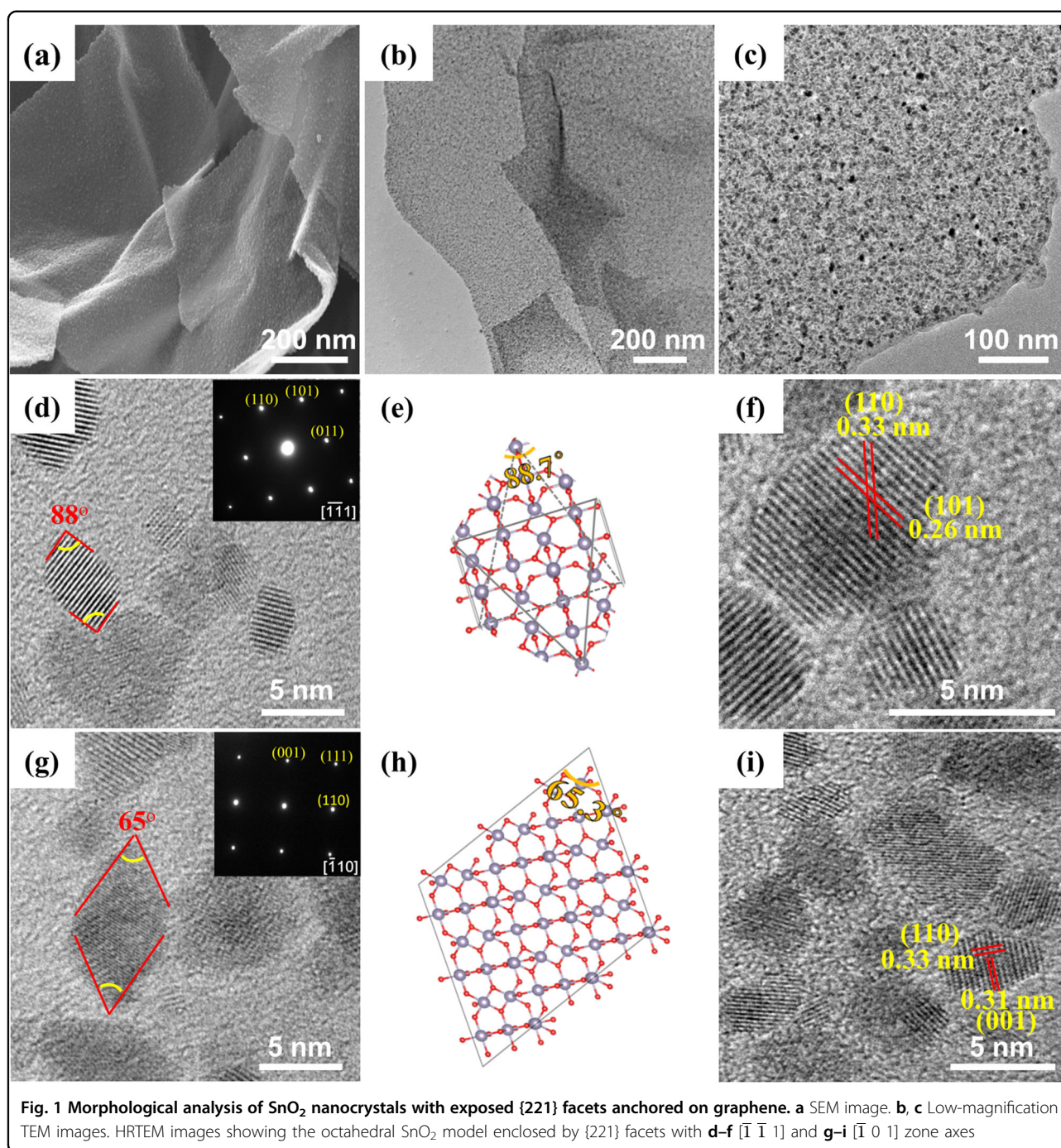
Fig. 1 Morphological analysis of SnO$_2$ nanocrystals with exposed {221} facets anchored on graphene. a SEM image. **b**, **c** Low-magnification TEM images. HRTEM images showing the octahedral SnO$_2$ model enclosed by {221} facets with **d–f** [$\bar{1}$ $\bar{1}$ 1] and **g–i** [$\bar{1}$ 0 1] zone axes

nanocrystals. Furthermore, to confirm the (physical or chemical) interaction between the SnO$_2$ nanocrystals and graphene, the obtained SnO$_2$/graphene nanocomposite was examined by XPS and FTIR spectroscopy. The overall XPS spectra reveal the presence of C1s, O1s, and Sn3d peaks (Supplementary Fig. S10a). The C1s peaks located at 284.5, 286.6, and 288.4 eV can be assigned to graphitic carbon, residual C–OH and O–C

= O, respectively (Fig. 2c). For the Sn3d spectrum, as shown in Supplementary Fig. S10b, the two symmetrical peaks observed at 486.6 eV and 495.5 eV are attributable to Sn 3d$_{5/2}$ and Sn 3d$_{3/2}$, respectively, indicating that the Sn atoms exist as SnO$_2$[50]. The observation of O1s peaks at 533.5 and 531.8 eV (Supplementary Fig. S10c) confirms the presence of carbonyl or hydroxyl groups and O^{2-} species in the SnO$_2$/graphene nanocomposite.
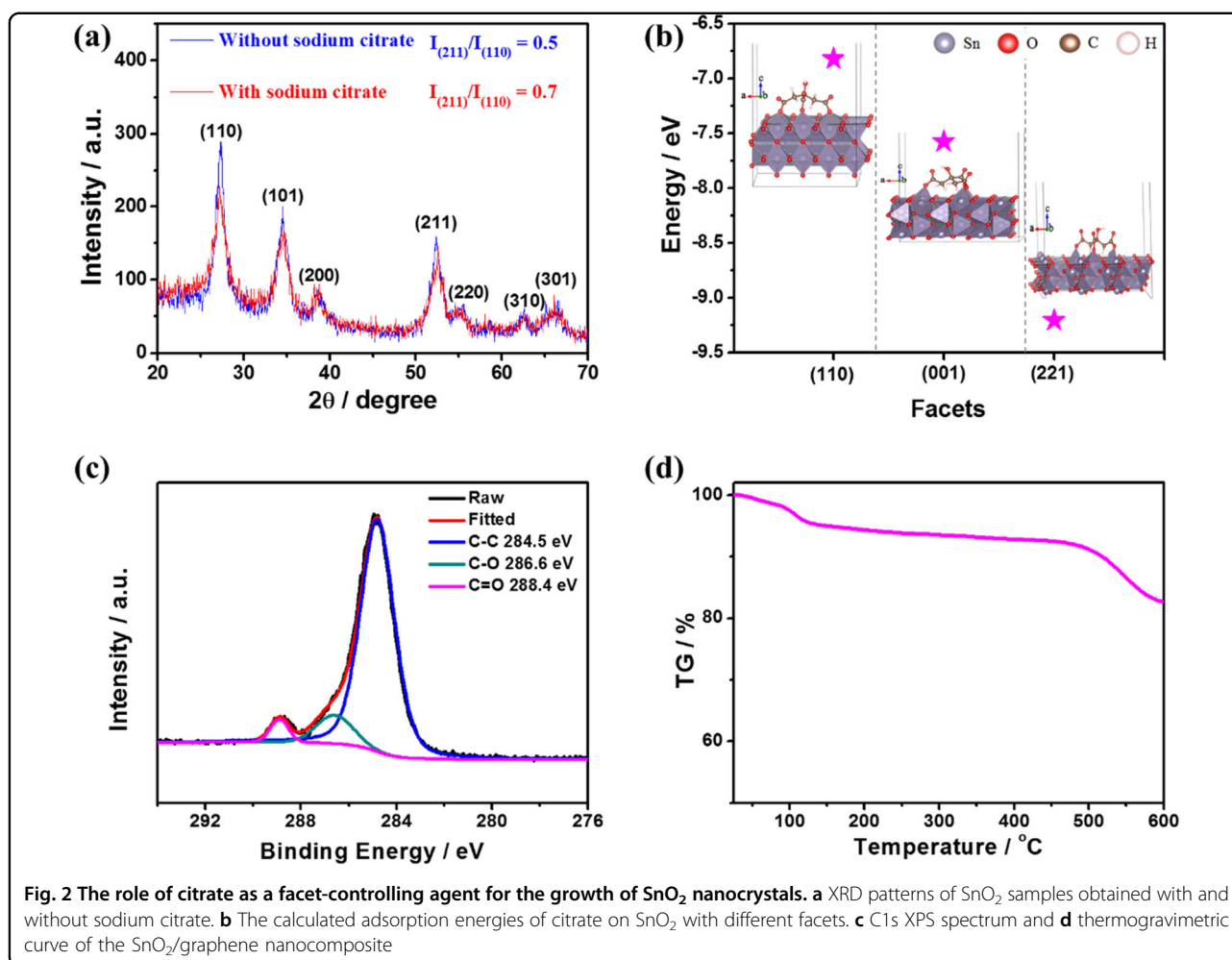
Fig. 2 The role of citrate as a facet-controlling agent for the growth of SnO₂ nanocrystals. a XRD patterns of SnO₂ samples obtained with and without sodium citrate. **b** The calculated adsorption energies of citrate on SnO₂ with different facets. **c** C1s XPS spectrum and **d** thermogravimetric curve of the SnO₂/graphene nanocomposite

A small amount of oxygenated groups is beneficial for achieving a high dispersion of SnO_2 nanocrystals on the graphene sheets through electrostatic interactions. In addition, strong Sn-O-Sn antisymmetric vibration peaks are observed in the FTIR spectrum at 604 and 563 cm^{-1} and assigned to the Eu mode of SnO_2 (Supplementary Fig. S10d). The absence of Sn–C, Sn–OOC, and Sn–O–C bonds in SnO_2/graphene indicates that the incorporation of SnO_2 nanocrystals on the graphene nanosheets is mainly based on physical adsorption. Meanwhile, the spectrum shows an absorption band at 1575 cm^{-1} corresponding to C = C stretching, indicating the restoration of the graphene network upon reduction. As indicated by the nitrogen adsorption and desorption isotherms (Supplementary Fig. S11), the Brunauer-Emmett-Teller specific surface area of the SnO_2/graphene nanocomposite is 215 $m^2 g^{-1}$, which is much higher than those of graphene nanosheets (87 $m^2 g^{-1}$) and SnO_2 nanoparticles (52 $m^2 g^{-1}$). The higher specific surface area of SnO_2/graphene compared with that of the graphene nanosheets proves again

that the SnO_2 nanocrystals enable independent dispersion of the graphene nanosheets without evident agglomeration. The thermogravimetric curve reveals that the weight ratios of graphene and SnO_2 nanocrystals in the composite are estimated to be 19 wt.% and 81 wt.%, respectively (Fig. 2d). As the positive electrode material, the morphology of the CNTs was characterized by SEM and HRTEM. The SEM images show that the length of the CNTs is in the range of several micrometers (Supplementary Fig. S12a–c). The fact that no O is detected combined with the clear interlayer distance of approximately 0.34 nm (Supplementary Fig. S12d–f) suggest a low oxidation and high degree of graphitization of the CNTs.

Before assembling the Na ion capacitor, the electrochemical behaviors of the CNTs (positive electrode) and the SnO_2 nanocrystals with exposed {221} facets anchored on graphene (negative electrode) were first investigated in half-cells using Na metal as both the counter and reference electrodes in the N-GPE. The galvanostatic charge–discharge (GCD) profiles of the CNTs exhibit a

typical symmetric triangular shape and almost straight lines at different current densities (Supplementary Fig. S13a), illustrating the characteristics of an electrochemical double-layer capacitor. At various sweep rates, the cyclic voltammetric (CV) curves of the CNTs show relatively flat rectangular shapes between 3.0 and 4.0 V (vs. Na^+/Na) and no Faradaic reaction (Supplementary Fig. S13b). The specific capacitance of the CNTs (Supplementary Fig. S14) at $0.5\,A\,g^{-1}$ is $173\,F\,g^{-1}$, and it remains at 162, 144, 115, and $72\,F\,g^{-1}$ when the current densities are increased to 0.6, 0.8, 1.2, and $1.8\,A\,g^{-1}$, respectively.

The GCD curves of the SnO_2/graphene nanocomposite present a sloping voltage profile without a clear voltage plateau, even at a low rate of 0.2 C (Fig. 3a). At a current density of $0.5\,A\,g^{-1}$, the specific capacitance of the SnO_2/graphene nanocomposite is as high as $276\,F\,g^{-1}$ and is maintained between 253 and $174\,F\,g^{-1}$ with increases in the charge–discharge current density from 0.6 to $1.2\,A\,g^{-1}$ (Fig. 3b). Even at a high current density of $1.8\,A\,g^{-1}$, a specific capacitance of $105\,F\,g^{-1}$ can still be maintained in the N-GPE. For comparison, the specific capacitances of the SnO_2 nanoparticles without graphene are obviously lower than those of SnO_2/graphene, which are in the range of $150–75\,F\,g^{-1}$ at current densities from $0.6\,A\,g^{-1}$ to $1.2\,A\,g^{-1}$ (Supplementary Fig. S15). Furthermore,

the cycling behavior of the SnO_2/graphene electrode tends to remain stable for 6000 cycles (Supplementary Fig. S16). To the best of our knowledge, this is one of the longest cycling lives observed to date among all reported metal oxide-based negative electrode materials for Na^+ storage[24–33].

Kinetic analysis based on CV tests from 1 to $200\,mV\,s^{-1}$ was carried out to determine the pseudocapacitive contribution to the total capacitance of the SnO_2/graphene nanocomposite. Unlike the reported SnO_2 nanoparticles and nanosheets with distinct redox peaks[52–55], the CV curves of the SnO_2/graphene nanocomposite at various sweep rates exhibit a broad anodic peak ranging from 0.1 to 3 V (vs. Na^+/Na) without visible cathodic peaks (Fig. 3c and Supplementary Fig. S17). In the voltage region from 0.9 to 0.1 V during the cathodic scan, Na^+ ions react with SnO_2 through conversion reactions (producing Sn and Na_2O) and alloying reactions (producing Na_xSn alloy)[55]. In the anodic portion, a dealloying reaction occurs, and the SnO_2 nanocrystals can be reverted to the original phase. These reversible reactions were previously revealed by TEM studies of SnO_2 nanocrystals[52,53]. Before the conversion reaction, Na^+ absorption within the SnO_2 nanocrystal takes places; thus, the migration path of Na ions was optimized, and the diffusion barrier (E_a) is only 0.19 eV (Supplementary Fig. S18). The change in current
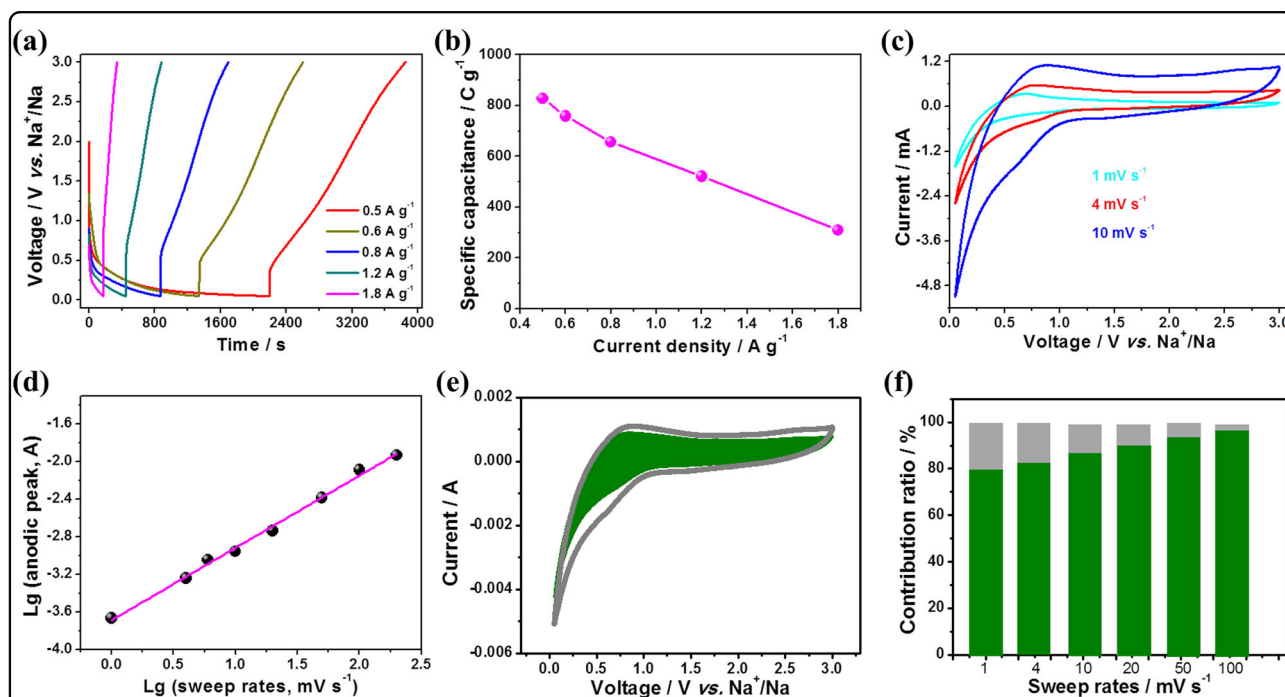

Fig. 3 Electrochemical performance of the SnO_2 nanocrystals with exposed {221} facets anchored on graphene (negative electrode) in half-cells. a GCD curves. **b** The corresponding specific capacitances at various current densities. **c** CV curves and **d** the Lg (anodic currents) vs. Lg (sweep rates). **e** Separation of the capacitive (green) and diffusion currents in SnO_2/graphene at a sweep rate of $10\,mV\,s^{-1}$. **f** Normalized contribution ratios of the capacitive (green) and diffusion-controlled (gray) capacitances at different sweep rates

with the sweep rate can be generally expressed as $i = a\nu^b$, where i is the current (A), ν is the sweep rate (mV s^{-1}) of a cyclic voltammetric experiment, and a and b are constants. A b value of 0.5 generally indicates a diffusion-controlled process, while a b value of 1.0 suggests that the reaction is surface-limited[34]. Here, the b value is approximately 0.8 even at the peak voltage (Fig. 3d), indicating that the kinetics are based on an interplay between surface- and diffusion-controlled reactions but are closer to surface-controlled diffusion. Additionally, the total current (i) resulting from capacitive effects ($k_1\nu$) and diffusion-controlled Faradic processes ($k_2\nu^{1/2}$) can be represented as:

$$i = k_1\nu + k_2\nu^{1/2} \qquad (2)$$

or

$$i/\nu^{1/2} = k_1\nu^{1/2} + k_2 \qquad (3)$$

After plotting $i/\nu^{1/2}$ versus $\nu^{1/2}$, one can determine the k_1 and k_2 values as well as the capacitive current contribution at a given voltage. Based on this quantification, 86% of the total charge (therefore, the capacitance) is capacitive at a scan rate of 10 mV s^{-1} (Fig. 3e). The diffusion-controlled charge is mainly generated near the peak voltage. The contribution ratios between pseudocapacitive storage and diffusion-controlled storage at other scan rates are illustrated in Figure 3f. With increasing scan rate, the capacitance from the diffusion-controlled reactions decreases faster than that from the capacitive effects, leading to an improvement in the capacitive contribution to the total stored charge. The capacitive contribution to the capacitance finally reaches a maximum value (92%) at the highest sweep rate of 100 mV s^{-1}.

The pseudocapacitive contribution mainly originates from the unique hybrid structure of SnO$_2$ nanocrystals with exposed high-energy facets anchored on graphene. First, the SnO$_2$ nanocrystals have ultrasmall sub-10 nm particle sizes. Actually, there have been reports that traditional battery materials exhibit capacitor-like properties at small dimensions (<10 nm)[56]. Second, the exposed highly reactive {221} facets in the SnO$_2$ nanocrystals may enhance the pseudocapacitive Na$^+$ storage behavior. First-principles calculations were performed to gain further insight into the sodiation dynamics of SnO$_2$ with different exposed facets. The optimized configurations of solvated Na$^+$ ions in diethylene glycol dimethyl ether (DEGDME) electrolyte are presented in Figure 4a. Each most stable Na$^+$ ion is coordinated by two DEGDME molecules in its primary solvation sheath, forming the complex cation Na$^+$(DEGDME)$_2$. Then, the interactions of three typical facets, {110} (Fig. 4b), {001} (Fig. 4c) and {221} (Fig. 4d), in SnO$_2$ with solvated Na$^+$ ions were considered. The {221} facet has the lowest surface

adsorption energy (-10.3 eV) compared with the {110} (-6.5 eV) and {001} (-8.4 eV) facets. This means that the {221} facet can realize the fastest and most stable adsorption of Na$^+$. During the conversion reaction with Na$^+$, part of the SnO$_2$ in the nanocrystals produces Sn and Na$_2$O, and then, the nearby Na$^+$ (adsorption on the {221} facets in unreacted SnO$_2$ nanocrystals) can easily react with the Sn to form Na$_x$Sn alloy, which greatly promotes the dynamics of the two-step conversion/alloying reaction. The presence of better overlap in the electron orbitals between Sn, Na, and O at the Fermi level of the {221} facets compared to that at the {110} and {001} facets, as shown in Supplementary Fig. S19, clearly demonstrates the interactions between the Sn, Na, and alloy atoms[57]. Third, the ultradispersed SnO$_2$ nanocrystals anchored on graphene provide abundant interfacial sites for Na$^+$ adsorption. Additional interfacial Na$^+$ storage usually occurs in the sub-10 nm SnO$_2$ nanocrystal–electrolyte, graphene–electrolyte and sub-10 nm SnO$_2$ nanocrystal–graphene interfaces[49,58]. Fourth, graphene can produce a nonfaradaic contribution from the electrical double-layer effect. The pure graphene electrode delivers a reversible capacitance of 45 F g^{-1} at 0.5 A g^{-1} (Supplementary Fig. S20), which is approximately 16% of the specific capacitance of the nanocomposite. Additionally, it should be noted that there are some essential electrochemical differences in the behavior of the SnO$_2$ electrode between Li$^+$ storage and Na$^+$ storage, which mainly involve different ion diffusivities, concentration-dependent moduli, and strengths between the lithiation and sodiation processes[55]. For example, the volume expansion for sodiation ($+9.6$ Å^3 for 1Na/8SnO$_2$) was much larger than that for lithiation ($+6.7$ Å^3, 1Li/8SnO$_2$)[55]. This essential electrochemical difference highlights another important role of graphene in eliminating the fragmentation and detachment of the SnO$_2$ electrode caused by volume expansion and contraction during Na$^+$ storage.

To assemble the quasi-solid-state Na ion capacitor (Fig. 5a), a gel polymer electrolyte (N-GPE) was utilized as both the separator and the electrolyte between the positive electrode (CNTs) and the negative electrode (SnO$_2$/graphene). Microsized pores ranging from 2 to 5 μm uniformly are distributed in the polymer matrix of the N-GPE (Supplementary Fig. S21). After calculation based on the equation $q = C_+ \times \Delta E_+ \times m_+ = C_- \times \Delta E_- \times m_-$ (where C is the specific capacitance in the half-cell test, ΔE is the voltage range, and m is the mass of the active material), the best mass ratio of the two electrodes (m_+/m_-) should be in the range of 3.6–3.8 (Fig. 5b). The voltage of the quasi-solid-state Na ion capacitor reaches 3.8 V, and its charge–discharge process is complete within 70 seconds at a high current density of 1.8 A g^{-1} (Fig. 5c). Along with the increase in the current density
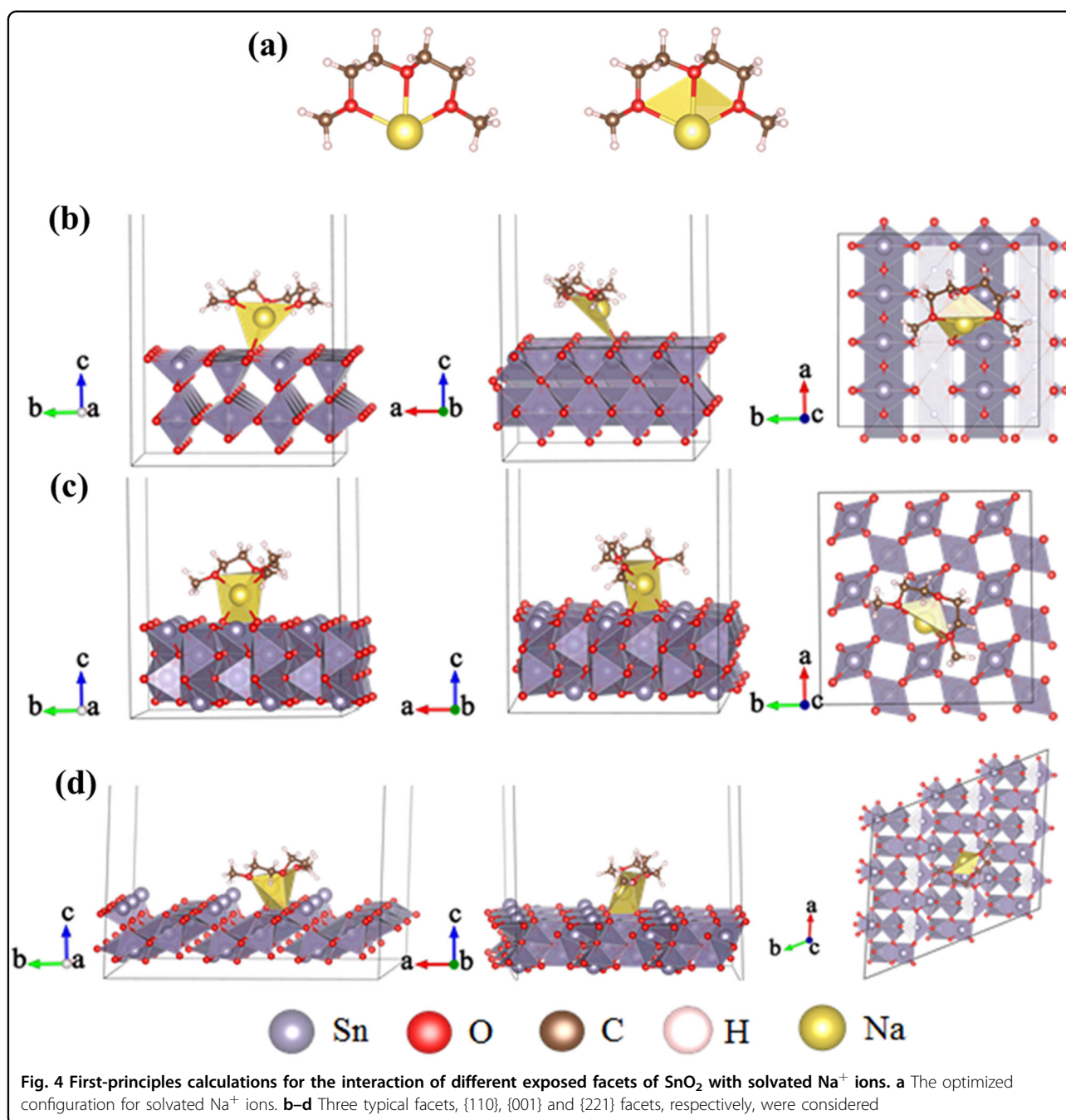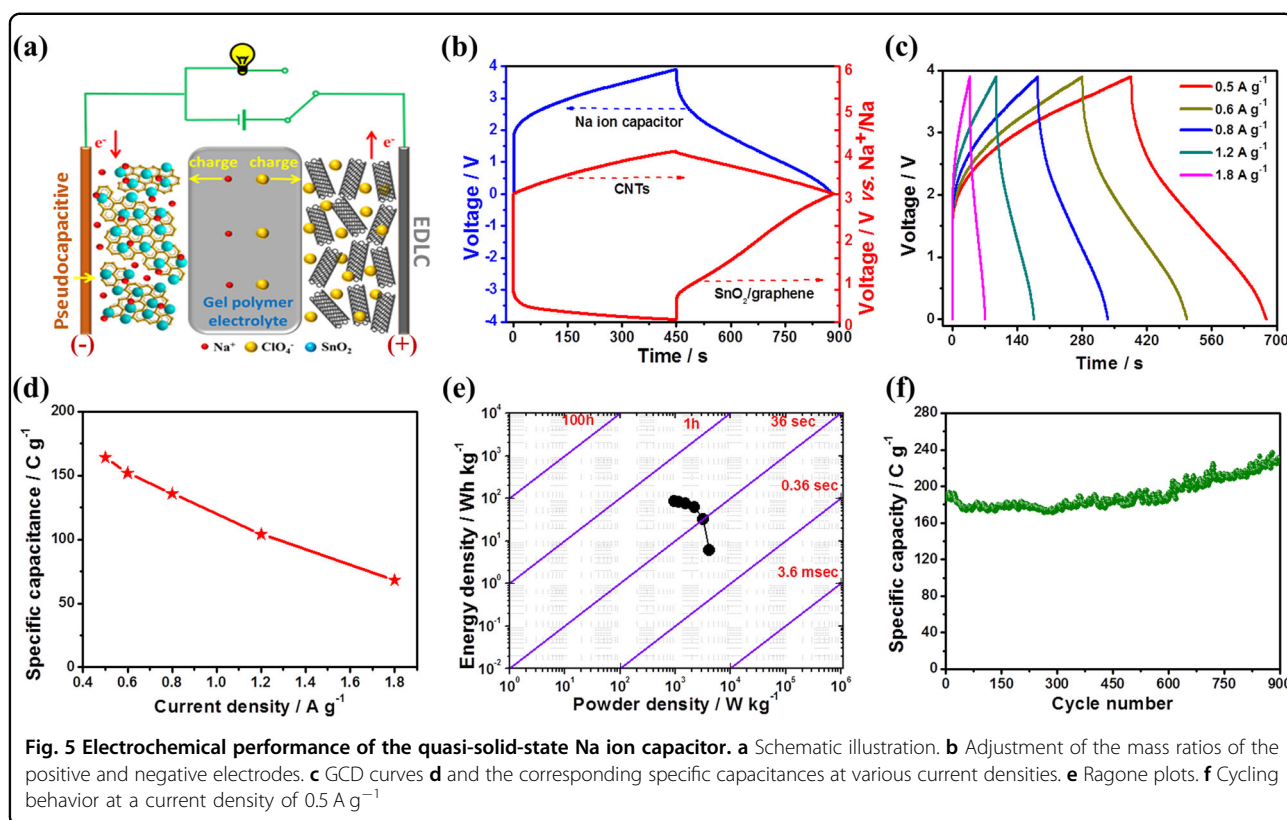
Fig. 4 First-principles calculations for the interaction of different exposed facets of SnO₂ with solvated Na⁺ ions. a The optimized configuration for solvated Na⁺ ions. **b–d** Three typical facets, {110}, {001} and {221} facets, respectively, were considered

from 0.5 A g^{-1} to 1.2 A g^{-1}, its specific capacitance decreases from 41 to 27 F g^{-1} based on the total weights of the negative and positive electrode materials (Fig. 5d). In addition, the quasi-solid-state Na ion capacitor shows a maximum energy density of 86 Wh kg^{-1} (at a power density of 955 W kg^{-1}) and a maximum power density of 4.1 kW kg^{-1} (Fig. 5e). The specific capacitance retains 100% of the initial value after 900 charge–discharge cycles at a current density of 0.5 A g^{-1} (Fig. 5f and Supplementary Fig. S22). The specific capacitance increases over the 900 cycles. Similarly, the measured capacitance also increases up to 2000 cycles in the half-cell (Supplementary Fig. S16a). To reveal the underlying reasons, post-cycling analysis of the SnO₂/graphene electrodes was carried out, and the results are shown in Supplementary Fig. S23. One of the reasons that can be determined is associated with the formation of a solid electrolyte interface (SEI) film on the surface of the SnO₂/graphene electrode and the "self-activation" of the formed SEI film during cycling. On the one hand,

Fig. 5 Electrochemical performance of the quasi-solid-state Na ion capacitor. a Schematic illustration. **b** Adjustment of the mass ratios of the positive and negative electrodes. **c** GCD curves **d** and the corresponding specific capacitances at various current densities. **e** Ragone plots. **f** Cycling behavior at a current density of 0.5 A g^{-1}

the irreversible reaction of electrolyte decomposition (producing NaF, Na$_2$CO$_3$, etc.) cannot be prevented in this voltage range (Supplementary Fig. S23a–c). The initial SEI film exhibits a relatively large charge transfer resistance (Supplementary Fig. S23d). On the other hand, the formation of an SEI film on the anode surface is necessary for maintaining its stability. The stable SEI film formed after the first hundreds of cycles could suppress further decomposition of the NaPF$_6$-based electrolyte but still enable the transport of Na$^+$ ions[59,60]. Compared with the initial SEI film formed during the first cycles, the stable SEI films formed after 300 cycles and 500 cycles have lower charge transfer resistances (Supplementary Fig. S23e–h). Such "self-activation" of the SEI film that formed on the SnO$_2$/graphene electrode could potentially be the origin of the observed continuous increase in capacitances during the initial cycles in the half-cell (Supplementary Fig. S16a) and the full Na ion capacitor (Fig. 5f). In addition, the gradual electrolyte wetting of the SnO$_2$/graphene electrode and the CNT electrode may also lead to an increase in the specific capacitance[61]. After being charged, the quasi-solid-state Na ion capacitor can readily power a commercial white light-emitting diode (Supplementary Fig. S24).

Generally, the reported quasi-solid-state Na ion capacitor described here provides significant progress, at least

in terms of the following three aspects. First, unlike the reported oxides such as Nb$_2$O$_5$ and RuO$_2$ with intrinsic pseudocapacitances[18,62], the reported SnO$_2$/graphene presents extrinsic pseudocapacitance when SnO$_2$ is made into ultrafine nanocrystals (sub-10 nm) with exposed {221} facets to maximize the reaction process on the surface. During the past several years, through the design of electrode materials with ordered mesopores or oxygen vacancies, researchers have discovered the existence of a pseudocapacitive contribution in some electrode materials for Li ion batteries[34–40]. Here, it is first demonstrated that nanocrystals (sub-10 nm) with exposed high-energy facets grown on graphene can induce pseudocapacitive Na$^+$ storage behavior. Thus, this work will enrich the methods for developing electrode materials with pseudocapacitive Na$^+$ storage behaviors. Second, most of previously reported Na ion capacitors are based on organic liquid electrolytes[24–30], which easily results in leakage of the electrolyte and serious safety issues. The electrochemical capacitors used in aqueous or ionic liquid electrolytes are well-known to be much more stable than Na ion batteries and not as susceptible to thermal run-away. However, this is not true for metal (Li or Na) ion capacitors because of the flammability of the organic electrolytes[31]. The matrix of our N-GPE shows a good flame-retarding ability. Due

to the presence of nonflammable functional groups (−C−F), the matrix does not catch fire when put in a flame although it shrinks (Supplementary Fig. S25)[63]. Moreover, replacing the liquid electrolyte with a gel polymer electrolyte does not lead to much of a decrease in the electrochemical performance of the Na ion capacitor and may improve the safety of electronic devices. Third, some high-index-faceted SnO_2 samples for gas-sensing and catalytic CO oxidation applications are currently available[51,64,65]. However, these SnO_2 samples with exposed high-energy facets have very large particle sizes (>100 nm)[51,64,65], which severely impedes their potential applications in electrochemical capacitors. The work described here is the first report of ultrasmall (sub-10 nm) SnO_2 nanocrystals enclosed within {221} high-index facets. In addition, the synthetic process for achieving ultradispersed sub-10 nm SnO_2 nanocrystals anchored on graphene is simple and can be easily scaled up. Such a highly efficient and low-cost preparation technology, together with the nonflammable electrolyte, provides great potential for the scale-up of quasi-solid-state Na ion capacitors for practical energy storage devices in the near future.

Conclusion

In summary, SnO_2 nanocrystals with a sub-10 nm size and exposed {221} facets are highly dispersed on graphene through a facile one-step reaction, and the resulting composite is further utilized as a negative electrode in a quasi-solid-state Na ion capacitor. We demonstrate that designing sub-10 nm SnO_2 nanocrystals with exposed high-energy facets anchored on graphene induces a surface-dominated redox reaction and a pseudocapacitive contribution to Na^+ storage. This pseudocapacitive ion storage behavior is highly beneficial for fast charge storage and excellent cyclability in a quasi-solid-state Na ion capacitor. In addition to SnO_2, the reported strategy may also work in other metal oxides for pseudocapacitive sodium-ion storage.

Author details
[1]State Key Laboratory of Materials-Oriented Chemical Engineering, Nanjing Tech University, Nanjing 210009 Jiangsu Province, China. [2]State Key Laboratory of Chemical Resource Engineering, Beijing University of Chemical Technology, Beijing 100029, China. [3]Institute for Advanced Materials, School of Energy Science and Engineering, Nanjing Tech University, Nanjing 211816 Jiangsu Province, China. [4]College of Mechanical and Electrical Engineering, Beijing University of Chemical Technology, Beijing 100029, China. [5]State Key Laboratory of Electroanalytical Chemistry, Changchun Institute of Applied Chemistry, Chinese Academy of Sciences, Changchun 130022 Jilin, China. [6]Faculty of Production Engineering, University of Bremen, 28359 Bremen, Germany

References
1. Chodankar, N., Dubal, D., Kwon, Y. & Kim, D. Direct growth of $FeCo_2O_4$ nanowire arrays on flexible stainless steel mesh for high-performance asymmetric supercapacitor. *NPG Asia Mater.* **9**, e419 (2017).
2. Aravindan, V., Gnanaraj, J., Lee, Y. S. & Madhavi, S. Insertion-type electrodes for nonaqueous Li-ion capacitors. *Chem. Rev.* **114**, 11619–11635 (2014).
3. Zhang, F. et al. A high-performance supercapacitor-battery hybrid energy storage device based on graphene-enhanced electrode materials with ultrahigh energy density. *Energy Environ. Sci.* **6**, 1623–1632 (2013).
4. Chen, Z. et al. 3D nanocomposite architectures from carbon-nanotube-threaded nanocrystals for high-performance electrochemical energy storage. *Adv. Mater.* **26**, 339–345 (2014).
5. Stoller, M. et al. Activated graphene as a cathode material for Li-ion hybrid supercapacitors. *Phys. Chem. Chem. Phys.* **14**, 3388–3391 (2012).
6. Zhang, T. et al. High energy density Li-ion capacitor assembled with all graphene-based electrodes. *Carbon N. Y.* **92**, 106–118 (2015).
7. Wang, F. et al. A quasi-solid-state Li-ion capacitor with high energy density based on Li_3VO_4/carbon nanofibers and electrochemically-exfoliated graphene sheets. *J. Mater. Chem. A* **5**, 14922–14929 (2017).
8. Ma, Y., Chang, H., Zhang, M. & Chen, Y. Graphene-based materials for lithium-ion hybrid supercapacitors. *Adv. Mater.* **27**, 5296–5308 (2015).
9. Ye, L. et al. A high performance Li-ion capacitor constructed with $Li_4Ti_5O_{12}$/C hybrid and porous graphene macroform. *J. Power Sources* **282**, 174–178 (2015).
10. Wang, Q., Wen, Z. H. & Li, J. H. A hybrid supercapacitor fabricated with a carbon nanotube cathode and a TiO_2-B nanowire anode. *Adv. Funct. Mater.* **16**, 2141–2146 (2006).
11. Puthusseri, D. et al. From waste paper basket to solid state and Li-HEC ultracapacitor electrodes: a value added journey for shredded office paper. *Small* **10**, 4395–4402 (2014).
12. Wang, F. et al. A quasi-solid-state Li ion capacitor based on porous TiO_2 hollow microspheres wrapped with graphene nanosheets. *Small* **12**, 6207–6213 (2016).
13. Leng, K. et al. Graphene-based Li-ion hybrid supercapacitors with ultrahigh performance. *Nano Res.* **6**, 581–592 (2013).
14. Wang, H., Guan, C., Wang, X. & Fan, H. A high energy and power Li-ion capacitor based on a TiO_2 nanobelt array anode and a graphene hydrogel cathode. *Small* **11**, 1470–1477 (2015).
15. Gokhale, R. et al. Oligomer-salt derived 3D, heavily nitrogen doped, porous carbon for Li-ion hybrid electrochemical capacitors application. *Carbon N. Y.* **80**, 462–471 (2014).
16. Yu, X. et al. Ultrahigh-rate and high-density lithium-ion capacitors through hybriding nitrogen-enriched hierarchical porous carbon cathode with prelithiated microcrystalline graphite anode. *Nano Energy* **15**, 43–53 (2015).
17. Wang, F. et al. Nanoporous $LiMn_2O_4$ spinel prepared at low temperature as cathode material for aqueous supercapacitors. *J. Power Sources* **242**, 560–565 (2013).
18. Augustyn, V., Simon, P. & Dunn, B. Pseudocapacitive oxide materials for high-rate electrochemical energy storage. *Energy Environ. Sci.* **7**, 1597–1614 (2014).

19. Dsoke, S., Fuchs, B., Gucciardi, E. & Wohlfahrt-Mehrens, M. The importance of the electrode mass ratio in a Li-ion capacitor based on activated carbon and $Li_4Ti_5O_{12}$. *J. Power Sources* **282**, 385–393 (2015).

20. Banerjee, A. et al. MOF-derived crumpled-sheet-assembled perforated carbon cuboids as highly effective cathode active materials for ultra-high energy density Li-ion hybrid electrochemical capacitors (Li-HECs). *Nanoscale* **6**, 4387–4394 (2014).

21. Qu, W. et al. Combination of a SnO_2-C hybrid anode and a tubular mesoporous carbon cathode in a high energy density non-aqueous lithium ion capacitor: preparation and characterisation. *J. Mater. Chem. A* **2**, 6549–6557 (2014).

22. Wang, X. & Shen, G. Intercalation pseudo-capacitive $TiNb_2O_7$@carbon electrode for high-performance lithium ion hybrid electrochemical supercapacitors with ultrahigh energy density. *Nano Energy* **15**, 104–115 (2015).

23. Jain, A. et al. Activated carbons derived from coconut shells as high energy density cathode material for Li-ion capacitors. *Sci. Rep.* **3**, 3002 (2013).

24. Aravindan, V., Ulaganathana, M. & Madhavi, S. Research progress in Na-ion capacitors. *J. Mater. Chem. A* **4**, 7538–7548 (2016).

25. Chen, Z. et al. High-performance sodium-ion pseudocapacitors based on hierarchically porous nanowire composites. *ACS Nano* **6**, 4319–4327 (2012).

26. Ding, J. et al. Peanut shell hybrid sodium ion capacitor with extreme energy-power rivals lithium ion capacitors. *Energy Environ. Sci.* **8**, 941–955 (2015).

27. Wang, X. et al. Pseudocapacitance of MXene nanosheets for high-power sodium-ion hybrid capacitors. *Nat. Commun.* **6**, 6544–6549 (2015).

28. Dall'Agnese, Y., Taberna, P. L., Gogotsi, Y. & Simon, P. Two-dimensional vanadium carbide (MXene) as positive electrode for sodium-ion capacitors. *J. Phys. Chem. Lett.* **6**, 2305–2309 (2015).

29. Le, Z. et al. Pseudocapacitive sodium storage in mesoporous single-crystal-like TiO_2-graphene nanocomposite enables high-performance sodium-ion capacitors. *ACS Nano* **11**, 2952–2960 (2017).

30. Thangavel, R., Moorthy, B., Kim, D. & Lee, Y. Pushing the energy output and cyclability of sodium hybrid capacitors at high power to new limits. *Adv. Energy Mater.* **7**, 1602654 (2017).

31. Wang, F. et al. A quasi-solid-state sodium-ion capacitor with high energy density. *Adv. Mater.* **27**, 6962–6968 (2015).

32. Li, H., Peng, L., Zhu, Y., Zhang, X. & Yu, G. Achieving high-energy high-power density in a flexible quasi-solid-state sodium ion capacitor. *Nano Lett.* **16**, 5938–5943 (2016).

33. Dong, S. et al. Self-supported electrodes of $Na_2Ti_3O_7$ nanoribbon array/graphene foam and graphene foam for quasi-solid-state Na-ion capacitors. *J. Mater. Chem. A* **5**, 5806–5812 (2017).

34. Brezesinski, T., Wang, J., Tolbert, S. & Dunn, B. Ordered mesoporous α-MoO_3 with iso-oriented nanocrystalline walls for thin-film pseudocapacitors. *Nat. Mater.* **9**, 146–151 (2010).

35. Brezesinski, K. et al. Pseudocapacitive contributions to charge storage in highly ordered mesoporous group V transition metal oxides with iso-oriented layered nanocrystalline domains. *J. Am. Chem. Soc.* **132**, 6982–6990 (2010).

36. Sathiya, M., Prakash, A., Ramesha, K., Tarascon, J. & Shukla, A. V_2O_5-anchored carbon nanotubes for enhanced electrochemical energy storage. *J. Am. Chem. Soc.* **133**, 16291–16299 (2011).

37. Augustyn, V. et al. Lithium-ion storage properties of titanium oxide nanosheets. *Mater. Horiz.* **1**, 219–223 (2014).

38. Lesel, B., Ko, J., Dunn, B. & Tolbert, S. Mesoporous $Li_xMn_2O_4$ thin film cathodes for lithium-ion pseudocapacitors. *ACS Nano* **10**, 7572–7581 (2016).

39. Kim, H. et al. Oxygen vacancies enhance pseudocapacitive charge storage properties of MoO_{3-x}. *Nat. Mater.* **16**, 454–460 (2017).

40. Huang, S. et al. Tunable pseudocapacitance in 3D $TiO_{2-\delta}$ nanomembranes enabling superior lithium storage performance. *ACS Nano* **11**, 821–830 (2016).

41. Wang, F. et al. *Nanoscale Horiz.* **1**, 272–289 (2016).

42. Chen, C. et al. Na^+ intercalation pseudocapacitance in graphene-coupled titanium oxide enabling ultra-fast sodium storage and long-term cycling. *Nat. Commun.* **6**, 6929–6936 (2015).

43. Chao, D. et al. Pseudocapacitive Na-ion storage boosts high rate and areal capacity of self-branched 2D layered metal chalcogenide nanoarrays. *ACS Nano* **10**, 10211–10219 (2016).

44. Chao, D. et al. Array of nanosheets render ultrafast and high-capacity Na-ion storage by tunable pseudocapacitance. *Nat. Commun.* **7**, 12122–12129 (2016).

45. Zhang, P. et al. One-step synthesis of large-scale graphene film doped with gold nanoparticles at liquid-air interface for electrochemistry and Raman detection applications. *Langmuir* **30**, 8980–8989 (2014).

46. Delley, B. An all-electron numerical method for solving the local density functional for polyatomic molecules. *J. Chem. Phys.* **92**, 508–517 (1990).

47. Blöchl, P. E. Projector augmented-wave method. *Phys. Rev. B* **50**, 17953–17979 (1994).

48. Halgren, T. & Lipscomb, W. The synchronous-transit method for determining reaction pathways and locating molecular transition states. *Chem. Phys. Lett.* **49**, 225–232 (1977).

49. Sun, Y. et al. Direct atomic-scale confirmation of three-phase storage mechanism in $Li_4Ti_5O_{12}$ anodes for room-temperature sodium-ion batteries. *Nat. Commun.* **4**, 1870–1880 (2013).

50. Li, Z. et al. High rate SnO_2-graphene dual aerogel anodes and their kinetics of lithiation and sodiation. *Nano Energy* **15**, 369–378 (2015).

51. Han, X. et al. Synthesis of tin dioxide octahedral nanoparticles with exposed high-energy {221} facets and enhanced gas-sensing properties. *Angew. Chem.* **121**, 9344–9347 (2009).

52. Su, D., Ahn, H. & Wang, G. SnO_2@graphene nanocomposites as anode materials for Na-ion batteries with superior electrochemical performance. *Chem. Commun.* **49**, 3131–3133 (2013).

53. Su, D., Wang, C., Ahn, H. & Wang, G. Octahedral tin dioxide nanocrystals as high capacity anode materials for Na-ion batteries. *Phys. Chem. Chem. Phys.* **15**, 12543–12550 (2013).

54. Ding, J. et al. Sodiation *vs.* lithiation phase transformations in a high rate-high stability SnO_2 in carbon nanocomposite. *J. Mater. Chem. A* **3**, 7100–7111 (2015).

55. Gu, M. et al. Probing the failure mechanism of SnO_2 nanowires for sodium–ion batteries. *Nano Lett.* **13**, 5203–5211 (2013).

56. Simon, P., Gogotsi, Y. & Dunn, B. Where do batteries end and supercapacitors begin? *Science* **343**, 1210–1211 (2014).

57. Su, D., Dou, S. & Wang, G. Gold nanocrystals with variable index facets as highly effective cathode catalysts for lithium-oxygen batteries. *NPG Asia Mater.* **7**, e155 (2015).

58. Chen, C. et al. Integrated intercalation-based and interfacial sodium storage in graphene-wrapped porous $Li_4Ti_5O_{12}$ nanofibers composite aerogel. *Adv. Energy Mater.* **6**, 1600322 (2016).

59. Yu, F. et al. The pseudocapacitance contribution in boron-doped graphite sheets for anion storage enables high-performance sodium-ion capacitors. *Mater. Horiz.* **3**, https://doi.org/10.1039/c8mh00156a (2018).

60. Wang, F. et al. Dual-graphene rechargeable sodium battery. *Small* **13**, 1702449 (2017).

61. Wang, J. et al. Graphene microsheets from natural microcrystalline graphite minerals: scalable synthesis and unusual energy storage. *J. Mater. Chem. A* **3**, 3144–3150 (2015).

62. Augustyn, V. et al. High-rate electrochemical energy storage through Li^+ intercalation pseudocapacitance. *Nat. Mater.* **12**, 518–522 (2013).

63. Zhu, Y. et al. Composite of a nonwoven fabric with poly(vinylidene fluoride) as a gel membrane of high safety for lithium ion battery. *Energy Environ. Sci.* **6**, 618–624 (2013).

64. Vayssieres, L. & Graetzel, M. Highly ordered SnO_2 nanorod arrays from controlled aqueous growth. *Angew. Chem. Int. Ed.* **43**, 3666–3670 (2004).

65. Sun, Y. et al. Atomically thin tin dioxide sheets for efficient catalytic oxidation of carbon monoxide. *Angew. Chem. Int. Ed.* **52**, 10569–10572 (2013).